Scattering phase matrix for hexagonal ice crystals computed from ray optics

Yoshihide Takano and Kolf Jayaweera

The scattering phase matrices for finite hexagonal cylinders oriented randomly in space were computed by superposing the scattered intensities of Fraunhofer diffracted rays and geometrical optics rays. However, the effect of interference is considered when the optical path lengths for two rays, split by some obstacle and scattered in the same direction, are equal to each other. Single models (c/a = 2.5 and 0.4) for a hexagonal column and a plate, resembling the corresponding crystals in atmospheric clouds, are used in the computations. Our results showed different values for the phase matrix elements, P_{33} and P_{44}, from those obtained previously by Cai and Liou. The backscattering linear depolarization ratios and the asymmetry factor for hexagonal plates oriented horizontally were then computed. The backscattering linear depolarization ratios exceeded 1.0 at certain orientations. Within the limitation of the use of single-crystal models for a hexagonal column and a plate, the results appear to agree well with most field and laboratory observations.

I. Introduction

The computational and theoretical studies on light scattering properties for ice crystals have been developed by several researchers.[1–5] They used the geometric ray tracing method which is approximately valid when the crystal size relative to the wavelength is large. These computations[4,5] show that the phase matrix elements, P_{33} and P_{44}, for finite hexagonal cylinders oriented randomly in 3-D space are different from those for spheroidal particles[5,6] and from the measured ones for artificial ice crystals.[7]

In this paper, using the ray optics B technique proposed by Takano and Tanaka,[8] we extend the work of Cai and Liou[4] (CL) on the scattering phase matrix for finite hexagonal cylinders oriented randomly in space. Here ray optics B means that the scattered intensity of the Fraunhofer diffracted rays, the intensity of the externally reflected rays, and the intensities of the refracted rays after some internal reflections are superimposed by ignoring their phases. However, the effect of interference must be considered when the optical path lengths for two rays, split by some obstacle and scattered in the same direction, are equal regardless of the size of the cylinder. As shown later, we can obtain the backscattering linear depolarization ratios and the asymmetry factor for randomly oriented hexagonal plates with vertical c axes when the phase matrix for the plates oriented randomly in space is computed. The computed backscattering linear depolarization ratios can then be compared with the lidar observations[9–11] and the laboratory measurements.[12,13] These results are applicable to remote sensing of atmospheric ice crystals.

II. Ray Tracing and Amplitude Matrix

In this study, when we do not explain a term, the notation of CL is being followed.

Let a plane wave be incident on a finite hexagonal cylinder from a direction with zenith angle $\eta = \pi/2 - \alpha$ and azimuth angle β measured with respect to the coordinate system fixed to the cylinder. The X and Z axes of this coordinate system are directed, respectively, along the a and c axes of the crystal, as shown in Fig. 1(a). Although CL have taken their X axis along the b axis of the crystal, such a minor difference will not affect the following discussion. As for the Cartesian coordinate system $OX'Y'Z'$, we apply a definition different from that of CL to reduce the number of integration for particle orientation. Although the axis OZ' is taken along the incident direction, the axis OX' is taken in the plane containing the axes OZ and OZ' as also shown in Fig. 1(a). Then the matrix $\mathbf{A}$ which represents the direction cosine between the six axes of $OXYZ$ and $OX'Y'Z'$ can be explicitly given by

$$\mathbf{A} = \begin{bmatrix} -\sin\alpha & 0 & \cos\alpha \\ 0 & 1 & 0 \\ -\cos\alpha & 0 & -\sin\alpha \end{bmatrix} \begin{bmatrix} \cos\beta & \sin\beta & 0 \\ -\sin\beta & \cos\beta & 0 \\ 0 & 0 & 1 \end{bmatrix}. \quad (1)$$

Both authors were with University of Alaska, Geophysical Institute, Fairbanks, Alaska 99775-1240 when this work was done; Y. Takano is now with University of Utah, Department of Meteorology, Salt Lake City, Utah 84112.

Received 2 March 1985.
0003-6935/85/193254-10$02.00/0.

Hereafter rays are traced by using the method of CL. {However, their Eq. (24) has been erroneously written and should be read as

$$\begin{bmatrix}\cos\chi_n\\ \cos\psi_n\\ \cos\omega_n\end{bmatrix} = [\Phi_1 D_1^t \Phi_2 D_2^r \cdots \Phi_{n-1} D_{n-1}^r] * A \begin{bmatrix}\cos\alpha_n\\ \cos\beta_n\\ \cos\gamma_n\end{bmatrix}, \quad n \geq 2. \tag{2}$$

Here the matrix with the asterisk $*$ represents the transposed matrix.}

The electric field vector $\mathbf{E}_n^{r,t}$ obtained by CL has been described in the coordinate system $OX_n^{r,t}Y_n^{r,t}Z_n^{r,t}$. Specifically, the plane $Z_n^{r,t}On_n$ in Fig. 1(b) is their reference plane to denote the electric field $\mathbf{E}_n^{r,t}$. On_n represents the outward normal direction of a prism plane. Here a prism plane refers to one of the rectangular sides of a finite hexagonal cylinder. So that the plane containing the propagation direction of the light ray and the Z axis becomes the reference plane, we rotate the coordinate system by the angle ϕ_{sn}. When a light ray emerges out of the basal planes of the crystal, their normal directions are parallel to the Z axis, and, therefore, $\phi_{sn} = 0$. Thus let us consider the case where a ray emerges out of a prism plane as shown in Fig. 1(b). Let the direction cosines of the three axes in the coordinate system $OX_n^{r,t}Y_n^{r,t}Z_n^{r,t}$ relative to the coordinate system $OXYZ$ be

$$B_{ij}^n = \cos\beta_{ij}^n, \qquad i,j = 1-3. \tag{3}$$

Then the matrix $\mathbf{B}^n$ is given by

$$\mathbf{B}^n = [\Xi_n^{r,t}] * \mathbf{A}. \tag{4}$$

From Fig. 1(b), the angle ϕ_{sn} is expressed as

$$\sin\phi_{sn} = \frac{\sin(\alpha_n - \rho_n)}{\sin\tau_n^{i,t}}, \tag{5}$$

$$\cos\phi_{sn} = -\frac{1}{\tan\beta_{33}^n \tan\tau_n^{i,t}}, \tag{6}$$

where

$$\rho_n = \mathrm{sgn}(\cos\beta_{32}^n)\cos^{-1}(\cos\beta_{31}^n/\sqrt{1-\cos^2\beta_{33}^n}), \tag{7}$$

$$\tau^{i,t} = \begin{cases}\tau_1^i, & \text{for } n = 1,\\ \tau_n^t, & \text{for } n \geq 2.\end{cases} \tag{8}$$

Thus the scattering amplitude matrix $\mathbf{A}'$ relative to the plane containing the propagation direction of the ray and the Z axis is expressed as

$$\mathbf{A}'^{(n)} = \begin{cases} w_1' \mathbf{P}_{s1}\mathbf{R}_1\mathbf{P}_1, & \text{for } n = 1,\\ w_n' \mathbf{P}_{sn}\mathbf{T}_n\mathbf{P}_n\left(\prod_{k=n-1}^{2}\mathbf{R}_k\mathbf{P}_k\right)\mathbf{T}_1\mathbf{P}_1, & \text{for } n \geq 2,\end{cases} \tag{9}$$

where

$$[w_n']^2 = \begin{cases}\dfrac{\cos\tau_1^i}{\sin\theta_1}, & \text{for } n = 1,\\ \dfrac{\cos\tau_1^i}{\sin\theta_n}\dfrac{\cos\tau_n^t}{\cos\tau_n^i}\dfrac{\cos\tau_1^t}{\cos\tau_1^i}\exp\left(-2km_i\sum_{l=1}^{n-1}d_{l+1,l}\right), & \text{for } n \geq 2.\end{cases} \tag{10}$$

In Eq. (9), $\mathbf{P}_{sn}$ is the 2×2 matrix which represents the rotation of the coordinate axis by the angle ϕ_{sn} similar to $\mathbf{P}_n$. When $n - 1$ is smaller than 2,

$$\prod_{k=n-1}^{2}\mathbf{R}_k\mathbf{P}_k$$

in Eq. (9) should be regarded as the identity matrix. In Eq. (10), the factor $\cos\tau_1^i/\sin\theta_n$ is explicitly included. This factor is derived from the fact that the fluxes of incident radiant energy and scattered radiant energy are proportional to $\cos\tau_1^i$ and $\sin\theta_n$, respectively. When the incident ray grazes the cylinder, i.e., when $\theta_1 = 0$ in Eq. (10), w_1' should be 1. As for $n \geq 2$, w_n' diverges when θ_n equals 0 or π as it does in the glory for large spherical particles. In such a case, the scattered intensity cannot be determined in the context of classical geometrical optics, so that $\sin\theta_n$ is then approximately given by $\sin(\Delta\theta/4)$, where $\Delta\theta$ is the numerical increment for the scattering angle, say 2°.

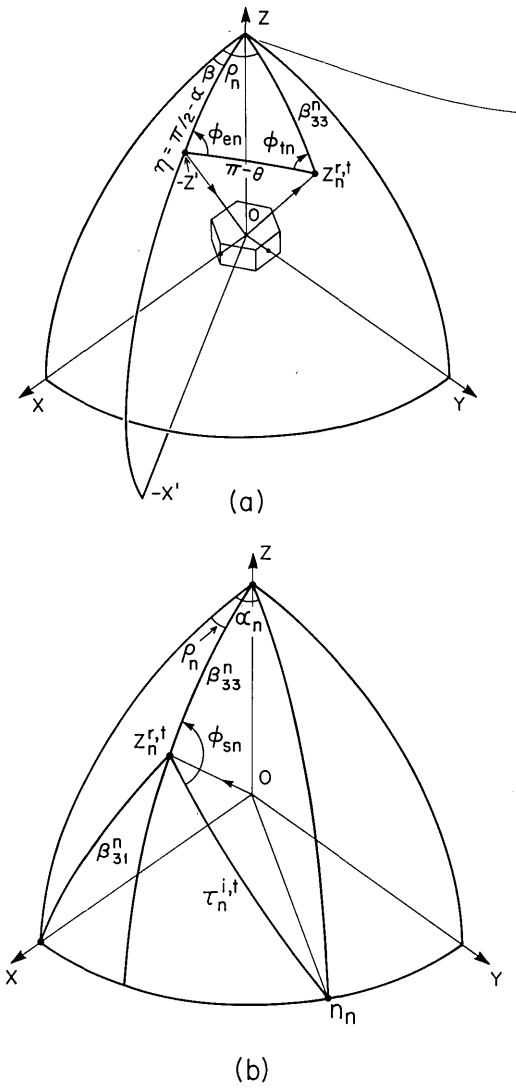

Fig. 1. (a) Scattering geometry for an incident light ray and a scattered light ray relative to a hexagonal ice crystal. (b) Scattering geometry for rotation of the coordinate system. All symbols are explained in the text.

Next, as known from the configuration in Fig. 1(a), the scattering amplitude matrix $\mathbf{A}^{(n)}$ in reference to the scattering plane can be given by

$$\mathbf{A}^{(n)} = \mathbf{P}_{tn}\mathbf{A}'^{(n)}\mathbf{P}_{-en}. \tag{11}$$

Here the angle ϕ_{en} is expressed as

$$\sin\phi_{en} = \frac{\sin\beta_{33}^{n}\sin(\rho_n - \beta)}{\sin\theta_n}, \tag{12}$$

$$\cos\phi_{en} = \frac{\cos\beta_{33}^{n} + \sin\alpha\cos\theta_n}{\sin\theta_n\cos\alpha}. \tag{13}$$

By interchanging β_{33}^{n} with $\pi/2 - \alpha$ in Eqs. (12) and (13), we can obtain the expressions for the angle ϕ_{tn}. For singular cases, the limit should be considered as follows:

$$\phi_{en} = \phi_{tn} = \pi/2 \qquad \text{for } \theta_n = 0 \text{ and } \pi. \tag{14}$$

III. Interference Between Two Rays

The scattering phase matrix $\mathbf{G}^{(n)}$ of the ray for n can generally be obtained from $\mathbf{A}^{(n)}$ regardless of the phase, as shown in the next section. However, let us consider that a plane wave encounters an obstacle, and two rays are split by the obstacle as shown in Figs. 2(b)–(d). The effect of interference should be considered when the two split rays are scattered in the same direction in space, and the optical path lengths are equal to each other regardless of the crystal size. In fact, such a situation can occur at $\theta = 0$, $\pi - 2\alpha$, 2α, and π in the plane including the Z axis and the incident direction as shown schematically in Figs. 2(a)–(d). When a ray is reflected at the basal planes an odd number of times, the ray is scattered at $\theta = \pi$ as in (b) or at $\theta = 2\alpha$ as in (c). When a ray is reflected at the basal planes an even number of times, the ray is scattered at $\theta = \pi - 2\alpha$ as in (b) or at $\theta = 0$ as in (c). Figure 2(d) represents a ray scattered at $\theta = \pi$. This ray is reflected once at the basal plane when $\alpha \neq 0$ or is not reflected at the basal plane when $\alpha = 0$. On the other hand, as in (e), two rays, which overlap each other in the end view, are not split by an obstacle. In this case, the effect of interference need not be considered. Hereafter, for the sake of later discussion, we refer to the backscattered rays shown in Figs. 2(b), (d), and (e), respectively, as the symmetrical

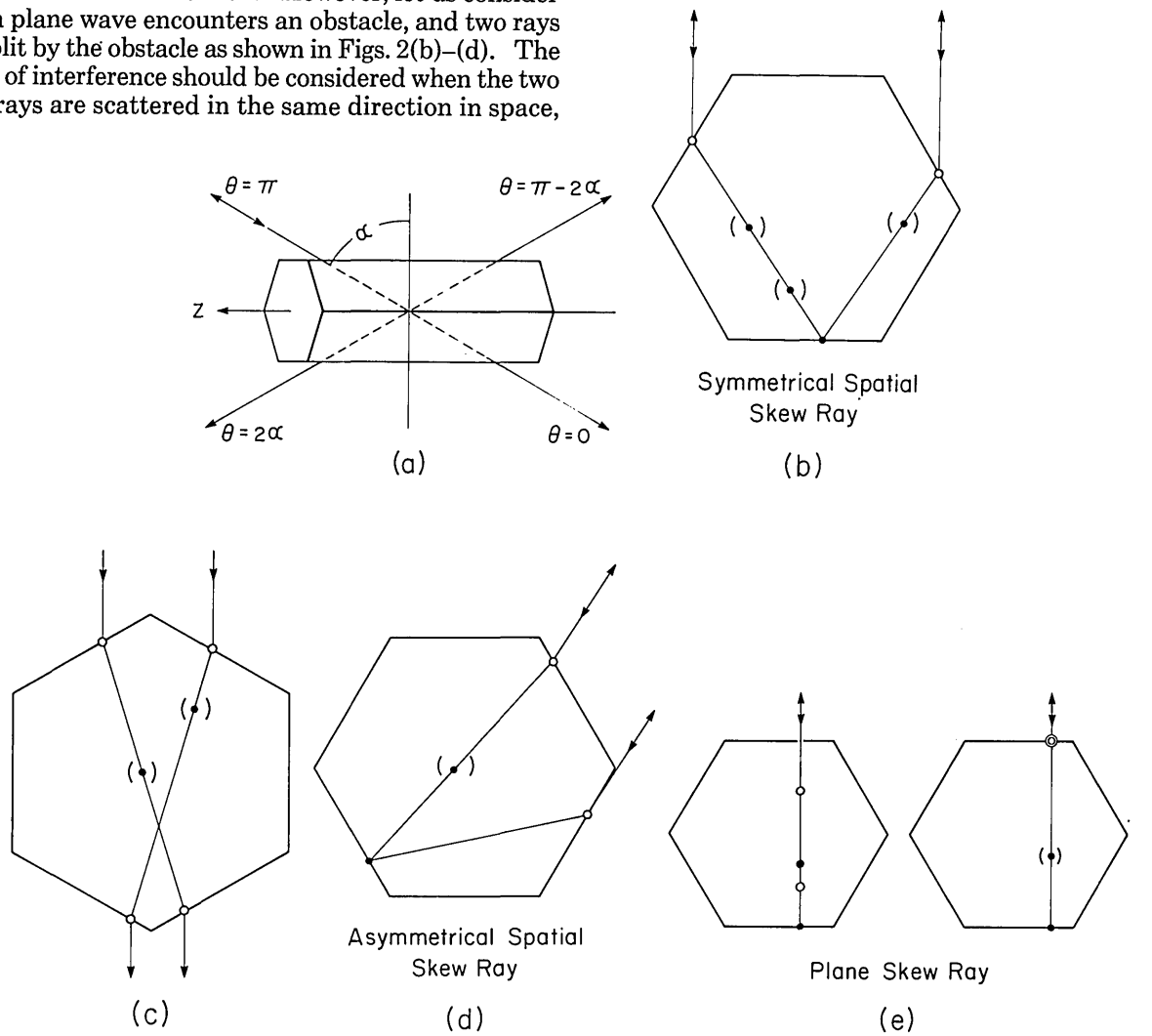

Fig. 2. (a) Schematic figure for the rays scattered at $\theta = 0, 2\alpha, \pi - 2\alpha$, and π in the plane containing the Z axis and the incident direction. (b)–(e) End views of a hexagonal cylinder and its light rays drawn in Fig. 2(a). Dot and circle represent reflection and refraction, respectively. Dot with parentheses denotes possible reflection. The left and right figures of (e), respectively, express a plane crystal and a columnar crystal.

spatial skew rays, the asymmetrical spatial skew rays, and the plane skew rays. The nomenclature of Liou and Lahore[2] is followed and extended here. Figure 2(e) corresponds to their Fig. 1.

In the case of the scattered light at $\theta = 0$, 2α, and $\pi - 2\alpha$ in Figs. 2(a)–(c), the relation between the amplitude matrices for the two interfering rays is the same as the relation between the amplitude matrices[14] for two particles which are mutually the mirror image with respect to the scattering plane. Thus the resultant amplitude matrix $\mathbf{S}^{(n)}$ is given by

$$\mathbf{S}^{(n)} = \begin{bmatrix} A_2^{(n)} & A_3^{(n)} \\ A_4^{(n)} & A_1^{(n)} \end{bmatrix} + \begin{bmatrix} A_2^{(n)} & -A_3^{(n)} \\ -A_4^{(n)} & A_1^{(n)} \end{bmatrix} = 2 \begin{bmatrix} A_2^{(n)} & 0 \\ 0 & A_1^{(n)} \end{bmatrix}. \quad (15)$$

This is because the signs of the rotational angles, $\phi_i (i = 1 - n)$ and ϕ_{sn}, of the coordinate system for these two interfering rays are opposite to each other similar to the corresponding case of a circular cylinder.[8]

On the other hand, in the case of $\theta = \pi$ in Figs. 2(b) and (d), the relation between the amplitude matrices for the two interfering rays is the same as the relation between the amplitude matrices[14] of two particles which are in the mutually reciprocal position with respect to the bisectrix. Thus the resultant amplitude matrix $\mathbf{S}^{(n)}$ is given by

$$\mathbf{S}^{(n)} = \begin{bmatrix} A_2^{(n)} & A_3^{(n)} \\ A_4^{(n)} & A_1^{(n)} \end{bmatrix} + \begin{bmatrix} A_2^{(n)} & -A_4^{(n)} \\ -A_3^{(n)} & A_1^{(n)} \end{bmatrix} = \begin{bmatrix} 2A_2^{(n)} & A_3^{(n)} - A_4^{(n)} \\ -[A_3^{(n)} - A_4^{(n)}] & 2A_1^{(n)} \end{bmatrix}. \quad (16)$$

Equation (16) shows the inherent property[14] in the amplitude matrix at $\theta = \pi$, that is, $S_3^{(n)} = -S_4^{(n)}$. The physical ground for Eq. (16) is given in the Appendix.

In fact, when we consider the phase matrix for ice crystals oriented randomly in space, many rays, whose interference can be discounted, contribute to the scattered intensities at $\theta = 0$, 2α, and $\pi - 2\alpha$, whereas the interfering rays exist only for $\alpha = \theta/2$ and $(\pi - \theta)/2$ at each scattering angle θ. So we might not adopt Eq. (15) for computation of the phase matrix at these directions in the case of random orientation in space. On the other hand, we should use Eq. (16) for the computation of the phase matrix at $\theta = \pi$ even in the case of random orientation in space, since the spatial skew rays as well as the plane skew rays exist for angles α.

IV. Scattering Phase Matrix for Finite Hexagonal Cylinders Oriented Randomly in Space

At first, by using the amplitude matrix $\mathbf{A}^{(n)}$ or $\mathbf{S}^{(n)}$ thus obtained, the phase matrix of the rays for n can be expressed in van de Hulst's notation[14] as

$$\mathbf{G}^{(n)} = \begin{bmatrix} \frac{1}{2}[M_2^{(n)} + M_3^{(n)} + M_4^{(n)} + M_1^{(n)}] & \frac{1}{2}[M_2^{(n)} - M_1^{(n)}] & 0 & 0 \\ \frac{1}{2}[M_2^{(n)} - M_1^{(n)}] & \frac{1}{2}[M_2^{(n)} - M_3^{(n)} - M_4^{(n)} + M_1^{(n)}] & 0 & 0 \\ 0 & 0 & S_{12}^{(n)} + S_{34}^{(n)} & -D_{21}^{(n)} \\ 0 & 0 & D_{21}^{(n)} & S_{12}^{(n)} - S_{34}^{(n)} \end{bmatrix}, \quad (17)$$

where the scattering angle is neither 0 nor π. Here we consider the phase matrix to transform the incident Stokes parameter (I_0, Q_0, U_0, V_0) to the scattered Stokes parameter (I, Q, U, V). By applying the assumption of rotational symmetry,[14] the phase matrix elements at $\theta = 0$ can be expressed as follows:

$$\left.\begin{aligned} G_{11}^{(n)} &= \tfrac{1}{2}[M_2^{(n)} + M_3^{(n)} + M_4^{(n)} + M_1^{(n)}], \\ G_{22}^{(n)} &= G_{33}^{(n)} = \tfrac{1}{4}[M_2^{(n)} - M_3^{(n)} - M_4^{(n)} + M_1^{(n)}] \\ &\quad + \tfrac{1}{2}[S_{12}^{(n)} + S_{34}^{(n)}], \\ G_{44}^{(n)} &= S_{12}^{(n)} - S_{34}^{(n)}, \end{aligned}\right\} \quad (18)$$

and the other G_{kl} values are 0. And at $\theta = \pi$, the nonzero matrix elements can be expressed as

$$\left.\begin{aligned} G_{11}^{(n)} &= \tfrac{1}{2}[M_2^{(n)} + 2M_3^{(n)} + M_1^{(n)}], \\ G_{22}^{(n)} &= -G_{33}^{(n)} = \tfrac{1}{4}[M_1^{(n)} + M_2^{(n)}] - \tfrac{1}{2}S_{12}^{(n)}, \\ G_{44}^{(n)} &= M_3^{(n)} + S_{12}^{(n)}. \end{aligned}\right\} \quad (19)$$

The above explicit representations for the phase matrix, Eqs. (17)–(19), are derived by following the method outlined by van de Hulst.

Next let us assume that the phase matrix can be approximately obtained by superposing not the amplitudes but the intensities when particles are oriented randomly in space. Thus the phase matrix elements can be expressed as the sum of the contribution from the Fraunhofer diffracted rays and those from the geometrical optics rays:

$$G_{kl}(m,ka,L/2a;\alpha,\beta;\theta,\phi) = \delta_{kl} G_D(ka,L/2a;\alpha,\beta;\theta,\phi) + \sum_q \left[\sum_{n=1}^{N} \delta(\theta - \theta_n, \phi - \phi_n) G_{kl}^{(n)}(m,ka,L/2a;\alpha,\beta;\theta_n,\phi_n) \right], \quad k,l = 1 - 4. \quad (20)$$

The diffraction term G_D for finite hexagonal cylinders is computed by the method described by Takano and Asano.[15] The summation for q in Eq. (20) is over each grid point on the finite hexagonal cylinder. If the material of the cylinder is nonabsorbing, the geometrical optics terms $G_{kl}^{(n)}$ in Eq. (20) become independent of the size parameter ka.

The phase matrix averaged over the angle β is expressed as

$$G_{kl}^{\beta}(m,ka,L/2a;\alpha;\theta) = \frac{6}{\pi} \int_0^{\pi/6} G_{kl}(m,ka,L/2a;\alpha,\beta;\theta,\phi) d\beta. \quad (21)$$

Here the above integration is performed regardless of the value of ϕ. Thus G_{kl}^{β} can be regarded as the phase matrix elements averaged not only over the angle β but also over the azimuthal angle ϕ. This integration

method to obtain G_{kl}^{β} is equivalent to the integration scheme of CL which rotates the cylinder around the incident direction. The backscattering linear depolarization ratios and the asymmetry factor for randomly oriented plate crystals with vertical c axes are obtained through Eq. (21). By integrating G_{kl}^{β} over the angle α, the phase matrix elements P_{kl} for ice crystals oriented randomly in space can be expressed as

$$P_{kl}(m;ka,L/2a;\theta) = \int_0^{\pi/2} G_{kl}^{\beta}(m;ka,L/2a;\alpha;\theta)\cos\alpha d\alpha. \quad (22)$$

V. Computed Results and Discussions

As several features of the computed scattering phase matrix for finite hexagonal cylinders have been explained by CL, we will mention only the features which are unexplained by them and different from them.

Figure 3 shows the phase function G_{11}^{β} averaged over the angles β and ϕ. This phase function corresponds to the azimuthally averaged one for randomly oriented hexagonal plates with vertical c axes at the solar elevation angle of 40°. In this case, we have considered up to five internal reflections, but the diffracted ray has not yet been included. The peak γ at $\theta = 28°$ corresponds to the 22° parhelia. The scattered intensity changes abruptly at $\theta = 100°$. This does not correspond to a certain peak but is only a discontinuity of intensity. Rays which are incident on a prism plane and emerge out of a prism plane after an even number of reflections at the basal planes are confined on a solid cone. This cone is the same as a parhelic circle. The angular diameter of the parhelic circle is $\pi - 2\alpha$. Hence there appears the abrupt reduction of the azimuthally averaged intensity at $\theta = 100°$. The peak δ at $\theta = 2\alpha = 80°$ corresponds to the subsun. The peaks ϵ and χ at $\theta =$ 86 and 134° correspond, respectively, to the 22° subparhelia and the 120° subparhelia, since these peaks are expected to appear, respectively, at $\theta = 86.58$ and 134.96° from simple geometry. Although the peak corresponding to the 120° parhelia would appear at θ = 83.12°, the strong intensity of the 22° subparhelia around $\theta = 86°$ masks the weak peak corresponding to the 120° parhelia. Thus the appearances of these well-known atmospheric optical phenomena indirectly assure the validity of our computation scheme. In addition, according to Greenler,[16] the 120° subparhelion has not yet been reported by anyone. However, the contrast between its azimuthally averaged intensity and the background intensity is stronger than the contrast between the intensity for the secondary rainbow and its background (e.g., Ref. 17). Therefore, we may be able to detect the 120° subparhelion from aircraft looking down into ice clouds.

Figures 4 and 5 show the six nonzero phase matrix elements for columns and plates oriented randomly in space (3-D columns and 3-D plates), respectively. The values of CL for wavelength λ, crystal shape ($L/2a$), and crystal size relative to the wavelength ($2\pi a/\lambda = ka$) are adopted for the sake of comparison. The inclusion of four internal reflections (i.e., $N = 6$) accounted for 97% of the total incident energy. The phase function is normalized so as to satisfy the following condition:

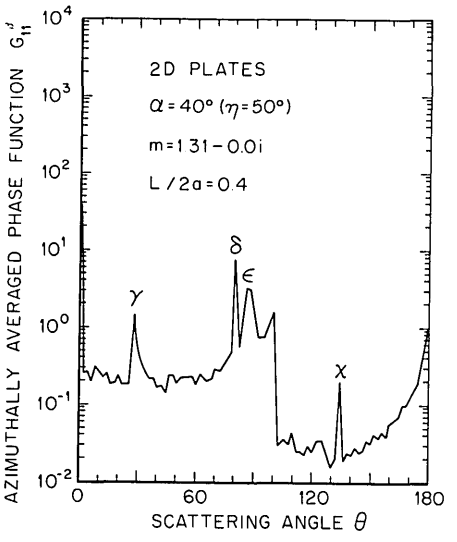

Fig. 3. Phase function averaged over the angles β and ϕ for randomly oriented hexagonal plates with vertical c axes (2-D plates) at the solar elevation angle of 40°.

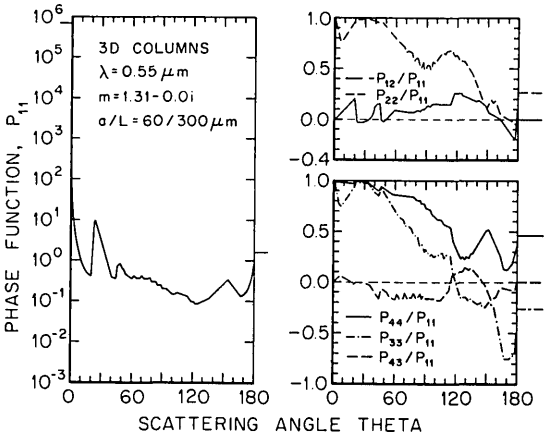

Fig. 4. Scattering phase matrix elements for hexagonal columns oriented randomly in space. The elements at the forward and backward scattering angles are indicated by short horizontal bars.

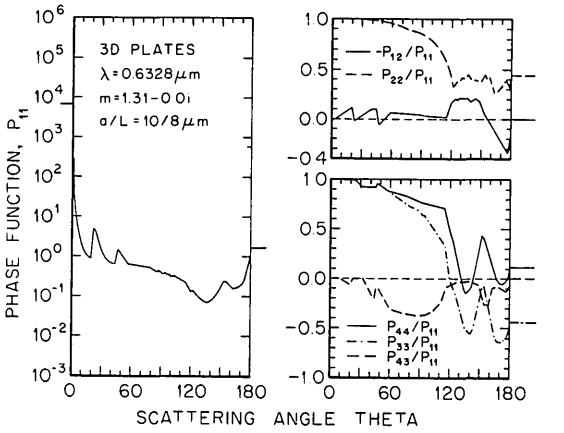

Fig. 5. Same as Fig. 4 except for hexagonal plates oriented randomly in space.

Table I. Asymmetry Factors Computed from Geometrical Optics and Backscattering Linear Depolarization Ratios for 3-D Columns, 3-D Plates, and Spheres[a]

	Column	Plate	Sphere
$(\overline{\cos\theta})_G$	0.5425	0.4169	0.8001
$((\overline{\cos\theta})_R)$	(0.7712)	(0.7084)	(0.9001)
$\delta_{H,V}(\theta = \pi)$	0.577	0.386	0.0

[a] The asymmetry factors for sufficiently large particles $(\overline{\cos\theta})_R$ are approximately computed through the relation $(\overline{\cos\theta})_R = [(\overline{\cos\theta})_G + 1]/2$.

$$\int_{4\pi} P_{11} d\Omega/4\pi = 1. \tag{23}$$

Comparing these figures with those of CL and LCBH,[5] we can see that the signs of the computed phase matrix elements P_{33} and P_{44} are opposite from theirs except for the forward scattering directions. As the behaviors of the computed phase matrix elements P_{33} and P_{44} resemble those for spheroids[5,6] and artificial ice crystals,[7] the phase matrix elements P_{33} and P_{44} in this study seem to be more accurate. In spite of the different size parameter, the computed phase matrix elements are closer to those of LCBH rather than those of CL at the scattering angles >90° where diffraction does not occur. They have computed the phase matrix for the monodisperse finite hexagonal cylinders by superposing the amplitudes. On the other hand, we compute the phase matrix by superposing the intensities under the assumption that the effect of the interference will be completely averaged out. Thus it turns out that the integration over the particle orientation has the effect of averaging out fluctuations on the scattered intensity due to interference, as does the integration over the particle size.[8]

In Figs. 4 and 5, we can see that $P_{11}(\theta = 22°)/P_{11}(\theta = 46°)$ for 3-D plates is smaller than that for 3-D columns as already pointed out by Pattloch and Tränkle.[18] Corresponding to this, the asymmetry factor $(\overline{\cos\theta})_G$ computed from geometrical optics for plates is smaller than that for columns (see Table I). The $(\overline{\cos\theta})_G$ values are independent of size parameter in this nonabsorbing case. Table I also shows that the asymmetry factors for ice crystals are smaller than that for spheres. This is because, in the case of finite hexagonal cylinders, the rays for $n = 2$ which would be scattered at forward scattering angles in the case of spheres[14,17] are often reflected totally and scattered at more backward scattering angles. A similar explanation can be seen for the asymmetry factor of smaller nonspherical particles.[19] This smaller asymmetry factor for finite hexagonal cylinders conforms with the fact that the observed cloud albedo for cirrus at the visible wavelength is larger than the cloud albedo computed under the assumption of spherical cloud particles.[20]

Next, let us consider the negative degree of linear polarization at near backward scattering directions ($\theta \simeq 178°$) in Figs. 4 and 5. Here let us refer to the two kinds of ray at near backward scattering directions as the near plane skew rays and the near spatial skew rays analogous to the corresponding rays at the backscattering direction in Sec. III. As the scattering plane hardly rotates in the case of near plane skew rays, $|A_1'^{(n)}|$ becomes greater than $|A_2'^{(n)}|$ because of the well-known property of the Fresnel reflection coefficients ($|R_{yn}| \geq |R_{xn}|$). On the other hand, in the case of near spatial skew rays, even if the scattering plane rotates, $|A_1'^{(n)}|$ is likely to be greater than $|A_2'^{(n)}|$, since $|R_{yn}| \geq |R_{xn}|$ too. The rotation of the coordinate system by $\phi_{en} \simeq \phi_{tn} \simeq \pi/2$ causes $|A_2^{(n)}|$ to be greater than $|A_1^{(n)}|$, and, therefore, the degree of linear polarization $-P_{12}/P_{11}$ has negative values as known from Eq. (17).

The nonzero phase matrix element P_{43} in Figs. 4 and 5 results from total reflection since $P_{43}^{(n)} = D_{21}^{(n)} = \mathrm{Im}[A_1^{(n)} A_2^{(n)*}]$. Here the asterisk denotes the complex conjugate. In the case of $\alpha = 0$, $P_{43}^{(3)}$ is always smaller than or equal to 0 because of the property of the Fresnel coefficients and the nonrotation of the incident plane. Thus as the phase matrix element P_{43} has negative values at $\alpha \simeq 0$, the element P_{43} for 3-D crystals is also likely to have negative values. However, this element P_{43} for 3-D columns has positive values at $116° \lesssim \theta \lesssim 144°$ in Fig. 4. These positive values for P_{43} are caused by the rays shown in Fig. 6(a) for $14° \lesssim \alpha \lesssim 26°$. In the case of 3-D plates, the flatness of the hexagonal plates

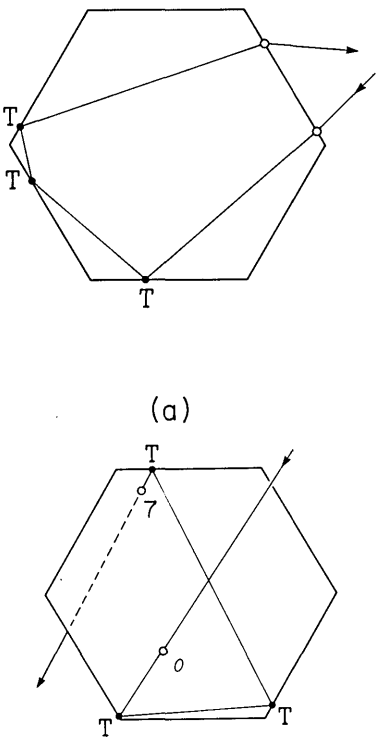

Fig. 6. (a) End view of a hexagonal column and a light ray causing the positive value of P_{43} at $116° \lesssim \theta \lesssim 144°$ in Fig. 4. T denotes total reflection. (b) End view of a hexagonal column and a light ray causing the large values of $\delta_{H,V}$ at $2° \lesssim \theta \lesssim 20°$ in Fig. 7. The digits 0 and 7 indicate the plane of incidence and plane of emergence, respectively.

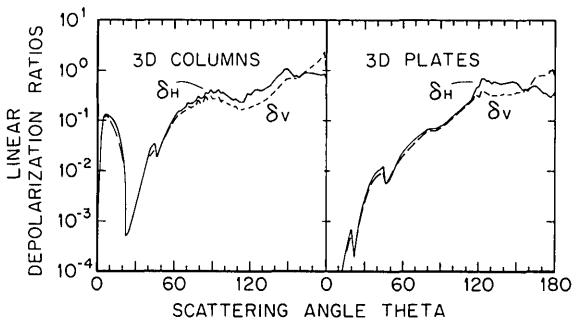

Fig. 7. Linear depolarization ratios δ_H and δ_V for 3-D columns and 3-D plates. The adopted parameters are the same as those in Figs. 4 and 5.

Table II. Main Contribution from Symmetrical Spatial Skew Rays to Backscattering[a]

Column			Plate		
α(deg)	Prism	Basal	α(deg)	Prism	Basal
			1–9	4(1)	6(3)
≤10	(Negligible)		10–34	4(1)	
11–57	4(1)		36–57	6(3)	
58–65	4(1)		58–76	6(1)	
66–77	4(1)	6(3)	≥77	(Negligible)	

[a] The digits 4 and 6 denote n. The digit in parentheses denotes the number of total reflections. Prism and Basal mean the plane on which the ray is incident. There are few contributions at $\alpha \gtrsim 78°$.

can cause a reflection from the basal plane of rays which travel in the path shown in Fig. 6(a) so that this feature does not appear in Fig. 5.

The matrix element P_{44}/P_{11} in Figs. 4 and 5 has a maximum value at $\theta = 152°$, which results from the fact that this element has a maximum value around there when $\alpha \simeq 0$. These maxima at $\alpha \simeq 0$ can be explained as follows. The positive values of this element at $\alpha \simeq 0$ are caused by the rays for $n = 4$ and $n = 5$, which are reflected totally once and reflected ordinarily once and twice, respectively. As the incident angles for the ordinary reflections are larger than the Brewster angle, the signs of R_{xn} and R_{yn} are the same. Hence $P_{44}^{(n)} \simeq P_{33}^{(n)} \simeq S_{12}^{(n)} = \mathrm{Re}[A_1^{(n)} A_2^{(n)*}]$ has positive values when $\alpha \simeq 0$. On the other hand, the background for P_{44}, caused by the externally reflected rays, has negative values since their incident angles are smaller than the Brewster angle. Therefore, the element P_{44}/P_{11} has maximum values around $\theta = 152°$ when $\alpha \simeq 0$.

Figure 7 shows the linear depolarization ratios δ_H and δ_V, which are defined, respectively, as

$$\delta_H = \frac{P_{11} - P_{22}}{P_{11} + 2P_{12} + P_{22}}, \tag{24}$$

$$\delta_V = \frac{P_{11} - P_{22}}{P_{11} - 2P_{12} + P_{22}}. \tag{25}$$

The linear depolarization ratio δ_V values for both 3-D columns and 3-D plates exceed 1.0 at near backward scattering directions ($\theta \simeq 178°$). The large values of the depolarization ratios for 3-D columns at $2° \lesssim \theta \lesssim 20°$ are caused by the rays as shown in Fig. 6(b) for $15° \lesssim \alpha \lesssim 45°$. However, the experimentally obtained δ_H and δ_V for columnar crystals (Fig. 3 of Ref. 21) do not show this strong depolarization in the forward scattering direction. This contradiction may be caused by the difference in size of each column ($L = 300$ μm and $\overline{L} \simeq 5$ μm). Namely, the peak of $\delta_{H,V}$ in Fig. 7 would be washed out by nondepolarized diffraction for small crystals.

In Table I, the backscattering linear depolarization ratios are also shown. These values are comparable with typical values, 0.3–0.5 for pure ice crystals observed by lidar.[10,11] The computed backscattering linear depolarization ratio for columns is larger than that for plates. This character can be explained as follows. Appreciable backscattering depolarization comes from spatial skew rays rather than from plane skew rays, since the incident planes do not rotate in the latter case. As shown in Table II, symmetrical spatial skew rays are incident mainly on prism planes in the case of both columns and plates. On the other hand, as shown in Fig. 2(e), plane skew rays are incident mainly on basal planes in the case of plates and on prism planes in the case of columns. Thus the ratio of the number of plane skew rays to the number of spatial skew rays for plates is larger than that for columns. Hence, in general, backscattering linear depolarization ratios for columns is likely to be larger than those for plates. In addition, we can explain this feature more specifically as follows. As shown in Table II, in the case of columns, the symmetrical spatial skew rays for $n = 4$ with one total reflection mainly cause the backscattering depolarization. On the other hand, in the case of plates, the symmetrical spatial skew rays for $n = 6$ with one total reflection cause the backscattering depolarization at $\alpha \geq 58°$. Figure 8 shows typical ray paths for symmetrical spatial

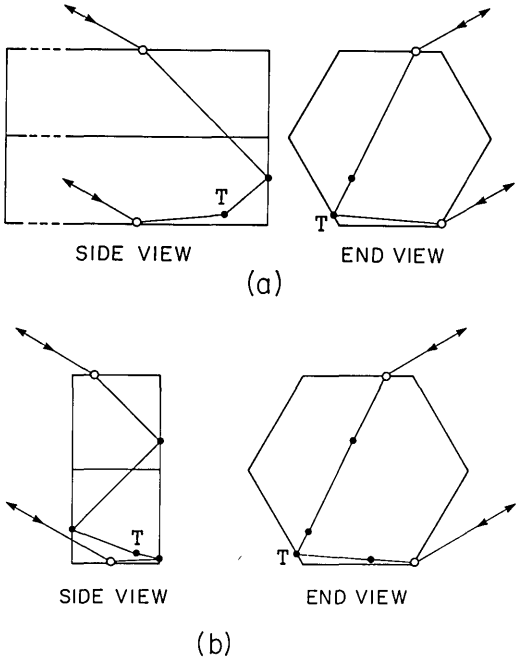

Fig. 8. Geometrical paths of symmetrical spatial skew rays at an orientation of $\alpha = 60°$ and $\beta = 30°$: (a) in the case of column ($L/2a = 2.5$) and $n = 4$; (b) in the case of plate ($L/2a = 0.4$) and $n = 6$.

skew rays which cause large depolarizations. From this figure, we can see that there can easily occur two more reflections at the basal planes in the case of plates since the shape of plate crystals is flatter than that of columnar crystals. These two extra reflections make the backscattered intensity of the symmetrical spatial skew rays for plates weaker than that for columns. On the other hand, plane skew rays for $n = 4$ contribute to backscattering in the case of both columns and plates. In fact, the backscattering linear depolarization ratios $\delta_H(\alpha)$ and $\delta_V(\alpha)$ for plates at each value of α behave as shown in Fig. 9, and these ratios for columns behave similar to those drawn in Fig. 9, but they take much larger values than those for plates at $\alpha \geq 58°$. Then the asymmetrical spatial skew rays for plates at $\alpha \lesssim 41°$ and those for columns at $\alpha \lesssim 51°$ contribute to backscattering. Thus the difference in the backscattering linear depolarization ratios between 3-D columns and 3-D plates in Table I stems especially from the difference in the symmetrical spatial skew rays at $\alpha \geq 58°$. Sassen[13] experimentally obtained larger values for backscattering linear depolarization ratios for columns than those for plates when strong intensities caused by single crystals were measured, although he obtained the value of ~0.5 for randomly oriented ice crystals in any of the crystal habits.[12] We infer that the intense single spikes in the former case[13] would have been caused by well-developed ice crystals which have clear optical faces in accordance with the assumption of the present study.

Figure 9 shows the backscattering linear depolarization ratios for randomly oriented plates with vertical c axes. As the assumption of the rotational symmetry is not valid, the depolarization ratios are then given by

$$\delta_H = \sum_n M_3^{(n)} \Big/ \sum_n M_1^{(n)}, \qquad \delta_V = \sum_n M_4^{(n)} \Big/ \sum_n M_2^{(n)}. \tag{26}$$

Here we take the plane containing the c axis and the direction of the incident light as the reference plane for polarization. We can see five different regions on the variation for δ_H and δ_V in this figure. These regions correspond to the five categories in Table II. Both δ_H and δ_V exceed 1.0 at $52° \leq \alpha \leq 59°$. This is because the sum of the rotational angles of the incident plane for the symmetrical spatial skew ray,

$$\sum_{i=1}^{n} \phi_i + \phi_{sn}$$

is close to 90° at these angles α. There are maximum values on δ_H and δ_V at $\alpha = 57°$. These maxima result from the following two reasons. The sum of the rotational angles for the incident plane,

$$\sum_{i=1}^{n} \phi_i + \phi_{sn}$$

is 90° at $\alpha \simeq 59°$, so that the ratios $M_3^{(n)}/M_1^{(n)}$ and $M_4^{(n)}/M_2^{(n)}$ for the symmetrical spatial skew rays themselves decrease at both $\alpha < 59°$ and $\alpha > 59°$. At $\alpha \geq 58°$, the number of total reflections for the symmetrical spatial skew rays decreases as shown in Table II, so that the scattered intensity of the symmetrical spatial skew

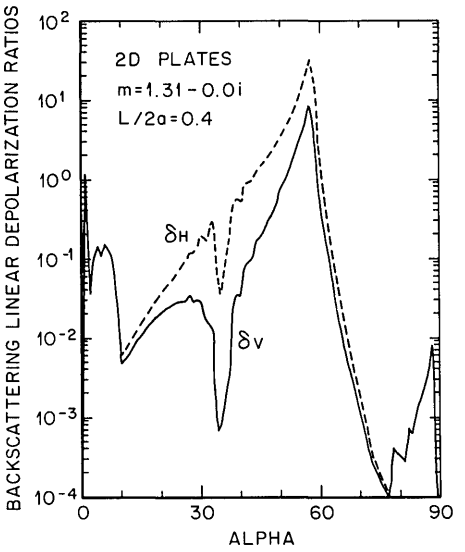

Fig. 9. Backscattering linear depolarization ratios δ_H and δ_V for randomly oriented hexagonal plates with vertical c axes as a function of the incident light direction α. The lidar tilt angle from the zenith is given by $\pi/2 - \alpha$.

rays relative to that of the plane skew rays also decreases. As a result, we can also see that the gradient of the decrease for δ_H and δ_V at $\alpha > 57°$ is steeper than that at $\alpha < 57°$.

Derr *et al.*[9] obtained the backscattering linear depolarization ratio >100% for a virga with the lidar tilted 30° from the zenith during nonturbulent conditions. If hexagonal plates with the c axes nearly vertical existed in that virga, their observed backscattering linear depolarization ratio corresponds to δ_V at $\alpha = 60°$ in Fig. 9. Although the value of δ_V at $\alpha = 60°$ is 0.511, the average values for δ_V are, respectively, 1.36 and 2.02, if δ_V is averaged over ±2 and ±3° around $\alpha = 60°$. This assumption approximately simulates the condition in which horizontally oriented plates fall wobbling with amplitudes between 2 and 3°. These wobbling angles are possible, since McDowell[22] reported that plate ice crystals, which cause the circumzenithal arc, undergo oscillation of around 1° from equilibrium. Thus the computed results shown in Fig. 9 fairly agree with their lidar observation. Moreover, from Fig. 9, we can infer that if Derr *et al.* had used a lidar tilt angle either smaller or much larger than 30° from the zenith, they might not have obtained a backscattering linear depolarization ratio of >100%.

On the other hand, Sassen[10] found anomalous δ values at $\alpha = 10$, 26, and 52° in virga. Although the observed δ at $\alpha = 52°$ is comparable with that in Fig. 9, those at $\alpha = 10$ and 26° are much larger than the computed ones in Fig. 9. This difference may stem from the effect of multiple scattering and/or the effect of crystal shape. However, this problem is still open.

Platt *et al.*[23] and Sassen[24] showed that the δ values rapidly increase as the lidar is scanned only 10° from the vertical. This behavior is also at variance with Fig. 9. However, a mixture of oriented and unoriented crystals present in the lidar beam would account for the above

difference. Figure 10 shows the corresponding variations in the parallel-polarized backscattered intensities,

$$M_{1,2} = \sum_n M_{1,2}^{(n)}$$

with the lidar elevation angle α. The strong intensity at $\alpha = 90°$ is caused by the specular reflection at the basal planes of the oriented plate crystals. Now let us assume that the backscattered intensity by the unoriented crystals is in the hatched region in Fig. 10. This value is generally determined by the ratio of the volume scattering coefficients of the oriented and unoriented crystals. Then, at $\alpha = 90°$, the lidar beam is scattered mainly by the oriented plate crystals, which explain the very small values of δ and the high returned powers. At $\alpha = 80°$ (or 82°), the lidar beam is scattered mainly by the unoriented crystals, which explain the observed values of δ (0.3–0.5) and the returned powers smaller than those at $\alpha = 90°$ by about 1 order of magnitude.

Figure 11 shows the dependence of the asymmetry factor $\overline{\cos\theta}$ of randomly oriented plates with a vertical c axes on the solar elevation angle α. At smaller values of α, say, $\alpha \lesssim 35°$, the asymmetry factor decreases with increasing α since the intensity of the 22° parhelion weakens and its position moves to larger scattering angles.[1] At $36° \leq \alpha \leq 57°$, as is well known, neither the circumzenithal arc nor the circumhorizontal arc appears because of the total reflection for the ray for $n = 2$, so that the asymmetry factor takes the smaller values. As the circumhorizontal arc begins to appear at $\alpha = 58°$ corresponding to the reduction of the number of total reflections, the asymmetry factor increases abruptly there.

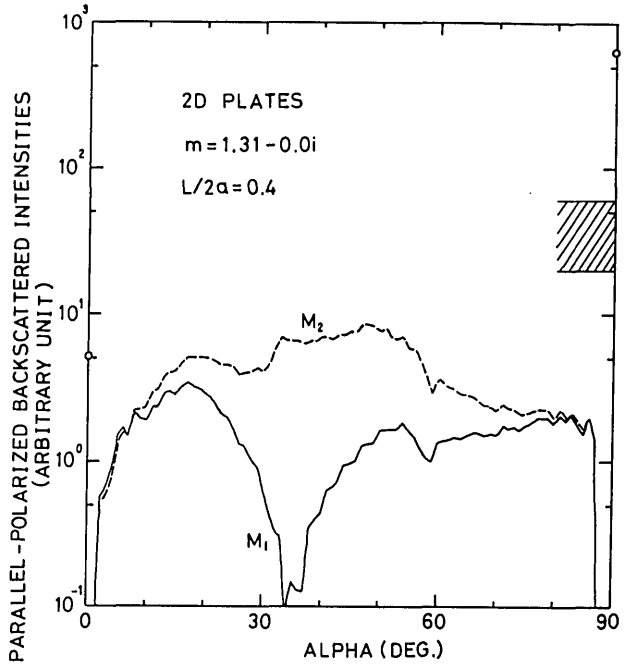

Fig. 10. Parallel-polarized backscattered intensities, M_1 and M_2, corresponding to Fig. 9 for randomly oriented hexagonal plates with vertical c axes as a function of the incident light direction α. The intensities at $\alpha = 0$ and 90° are indicated by open circles. The hatched region is the estimated backscattered intensities for the unoriented crystals.[23,24]

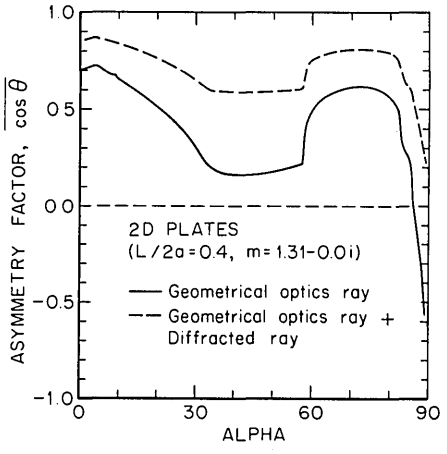

Fig. 11. Asymmetry factor for randomly oriented hexagonal plates with vertical c axes as a function of the solar elevation angle α. The dashed line $(\overline{\cos\theta})_R$ is obtained through the relation mentioned in Table I.

VI. Conclusions

The scattering phase matrices for finite hexagonal cylinders oriented randomly in space have been computed on the basis of geometrical optics principles. Computed results similar to those of Cai and Liou[4] and Liou *et al.*[5] have been obtained except for the phase matrix elements P_{33} and P_{44}. The matrix element P_{44} is greater than or equal to the matrix element P_{33}. The comparison of our computed phase matrix with those of CL[4] and LCBH[5] has also shown that the integration of the phase matrix over the particle orientation has the effect of averaging out the fluctuations on the scattered intensity due to interference, as also does the integration over the particle size parameter. However, the effect of interference must be taken into account when the optical path lengths for two rays, split by some obstacle and scattered in the same direction, are equal to each other regardless of the size of the crystal. The computed asymmetry factors for ice crystals oriented randomly in space have been smaller than that for the corresponding spheres.

The computed backscattering linear depolarization ratios for randomly oriented hexagonal plates with vertical c axes depend strongly on the direction of the incident light. And these ratios exceed 1.0 at certain orientations. This can be regarded as one possibility for the abnormally large values of δ_V for a virga observed by lidar.[9] The asymmetry factor for horizontally oriented plates varies considerably with the solar elevation angle.

Several computed scattering characteristics can be explained by atmospheric optical phenomena and in terms of the total reflection inherent in nonspherical particles. By using the computed phase matrix for 3-D ice crystals, we will be able to compute the polarization field as well as the intensity field in multiple scattering and by extending this study further to investigate the radiative properties of optically anisotropic ice clouds.[25]

Appendix

For the discussion below, let us express the amplitude matrix of rays scattered at $\theta = \pi$ as shown in Figs. 2(b) and (d) as

$$\mathbf{A}'^{(n)}/w_n' = \mathbf{P}_{sn}\mathbf{T}_n\mathbf{P}_n\left(\prod_{k=n-1}^{2}\mathbf{R}_k\mathbf{P}_k\right)\mathbf{T}_1\mathbf{P}_1 \equiv \begin{bmatrix} U_2 & U_3 \\ U_4 & U_1 \end{bmatrix}. \quad \text{(A1)}$$

Here we may not necessarily consider the matrix $\mathbf{A}^{(n)}$, since $\mathbf{A}^{(n)}$ is simply related to $\mathbf{A}'^{(n)}$ at $\theta = \pi$ as known from Eq. (14). If the above matrix is transposed, the following relation can be obtained:

$$\mathbf{P}_1^*\mathbf{T}_1\left(\prod_{k=2}^{n-1}\mathbf{P}_k^*\mathbf{R}_k\right)\mathbf{P}_n^*\mathbf{T}_n\mathbf{P}_{sn}^* = \begin{bmatrix} U_2 & U_4 \\ U_3 & U_1 \end{bmatrix}. \quad \text{(A2)}$$

By using the property

$$\mathbf{P}_n^* = \mathbf{P}_{-n}$$

and the aforementioned one, in which the sign of the nondiagonal elements of the amplitude matrix changes if the signs of rotational angles of the coordinate system are reversed, we can get

$$\mathbf{P}_1\mathbf{T}_1\left(\prod_{k=2}^{n-1}\mathbf{P}_k\mathbf{R}_k\right)\mathbf{P}_n\mathbf{T}_n\mathbf{P}_{sn} = \begin{bmatrix} U_2 & -U_4 \\ -U_3 & U_1 \end{bmatrix}. \quad \text{(A3)}$$

The left-hand side of Eq. (A3) is nothing other than the amplitude matrix for the ray whose propagation direction is opposite to that of the original ray whose amplitude matrix is given by Eq. (A1). At $\theta = \pi$, these two rays can interfere since their scattered directions coincide.

References

1. H. Jacobowitz, "A Method for Computing the Transfer of Solar Radiation through Clouds of Hexagonal Ice Crystals," J. Quant. Spectrosc. Radiat. Transfer **11**, 691 (1971).
2. K. N. Liou and H. Lahore, "Laser Sensing of Cloud Composition: A Backscattered Depolarization Technique," J. Appl. Meteorol. **13**, 257 (1974).
3. P. Wendling, R. Wendling, and H. K. Weickmann, "Scattering of Solar Radiation by Hexagonal Ice Crystals," Appl. Opt. **18**, 2663 (1979).
4. Q. Cai and K.-N. Liou, "Polarized Light Scattering by Hexagonal Ice Crystals: Theory," Appl. Opt. **21**, 3569 (1982).
5. K.-N. Liou, Q. Cai, P. W. Barber, and S. C. Hill, "Scattering Phase Matrix Comparison for Randomly Hexagonal Cylinders and Spheroids," Appl. Opt. **22**, 1684 (1983).
6. S. Asano and M. Sato, "Light Scattering by Randomly Oriented Spheroidal Particles," Appl. Opt. **19**, 962 (1980).
7. V. P. Dugin and S. O. Mirumyants, "The Light Scattering Matrices of Artificial Crystalline Clouds," Izv. Acad. Sci. USSR Atmos. Oceanic Phys. **12**, 988 (1976).
8. Y. Takano and M. Tanaka, "Phase Matrix and Cross Sections for Single Scattering by Circular Cylinders: a Comparison of Ray Optics and Wave Theory," Appl. Opt. **19**, 2781 (1980).
9. V. E. Derr, N. L. Abshire, R. E. Cupp, and G. T. McNice, "Depolarization of Lidar Returns from Virga and Source Cloud," J. Appl. Meteorol. **15**, 1200 (1976).
10. K. Sassen, "Polarization Diversity Lidar Returns from Virga and Precipitation: Anomalies and the Bright Band Analogy," J. Appl. Meteorol. **15**, 292 (1976).
11. A. I. Carswell, in *Clouds, Their Formation, Optical Properties, and Effects*, P. V. Hobbs and A. Deepak, Eds. (Academic, New York, 1981), pp. 363–406.
12. K. Sassen, "Depolarization of Laser Light Backscattered by Artificial Clouds," J. Appl. Meteorol. **13**, 923 (1974).
13. K. Sassen, "Ice Crystal Habit Discrimination with the Optical Backscatter Depolarization Technique," J. Appl. Meteorol. **16**, 425 (1977).
14. H. C. van de Hulst, *Light Scattering by Small Particles* (Dover, New York, 1981), pp. 44–55.
15. Y. Takano and S. Asano, "Fraunhofer Diffraction by Ice Crystals Suspended in the Atmosphere," J. Meteorol. Soc. Jpn. **61**, 289 (1983).
16. R. Greenler, *Rainbows, Halos, and Glories* (Cambridge U.P., New York, 1980), p. 80.
17. K. N. Liou and J. E. Hansen, "Intensity and Polarization for Single Scattering by Polydisperse Spheres: A Comparison of Ray Optics and Mie Theory," J. Atmos. Sci. **28**, 995 (1971).
18. F. Pattloch and E. Trankle, "Monte Carlo Simulation and Analysis of Halo Phenomena," J. Opt. Soc. Am. A **1**, 520 (1984).
19. J. B. Pollack and J. N. Cuzzi, "Scattering by Nonspherical Particles of Size Comparable to a Wavelength: A New Semi-Empirical Theory and Its Application to Tropospheric Aerosols," J. Atmos. Sci. **37**, 868 (1980).
20. C. M. R. Platt, "The Effect of Cirrus of Varying Optical Depth on the Extraterrestrial Net Radiative Flux," Q. J. R. Meteorol. Soc. **107**, 671 (1981).
21. K. Sassen and K. N. Liou, "Scattering of Polarized Laser Light by Water Droplet, Mixed-Phase and Ice Crystal Clouds. Part II: Angular Depolarizing and Multiple-Scattering Behavior," J. Atmos. Sci. **36**, 852 (1979).
22. R. S. McDowell, "Frequency Analysis of the Circumzenithal Arc: Evidence for the Oscillation of Ice-Crystal Plates in the Upper Atmosphere," J. Opt. Soc. Am. **69**, 1119 (1979).
23. C. M. R. Platt, N. L. Abshire, and G. T. McNice, "Some Microphysical Properties of an Ice Cloud from Lidar Observation of Horizontally Oriented Crystals," J. Appl. Meteorol. **17**, 1220 (1978).
24. K. Sassen, "Deep Orographic Cloud Structure and Composition Derived from Comprehensive Remote Sensing Measurements," J. Climate Appl. Meteorol. **23**, 568 (1984).
25. S. Asano, "Transfer of Solar Radiation in Optically Anisotropic Ice Clouds," J. Meteorol. Soc. Jpn. **61**, 402 (1983).

The authors are deeply indebted to K. Sassen for his valuable comments when refereeing this paper. The authors express their thanks to K. N. Liou and S. Asano for going through the first draft of this paper. One of the authors (Y. T.) is also grateful to W. Fuller for polishing his English. This research was supported by the Division of Atmospheric Sciences of the National Science Foundation under grant ATM 81-05065.